Cryo-EM and Molecular Dynamics Simulations Reveal Hidden Conformational Dynamics Controlling Ammonia Transport in Human Asparagine Synthetase

Adriana Coricello[1,9], Alanya. J. Nardone[2], Antonio Lupia[3,10], Carmen Gratteri[1], Matthijn Vos[4], Vincent Chaptal[5], Stefano Alcaro[1,3,*], Wen Zhu[2,*], Yuichiro Takagi[6,*] & Nigel G. J. Richards[7,8,*]

[1]Dipartimento di Scienze della Salute, Università "Magna Græcia" di Catanzaro, 88100 Catanzaro, Italy

[2]Department of Chemistry & Biochemistry, Florida State University, Tallahassee, FL 32306, USA

[3]Net4Science Academic Spin-Off, Università "Magna Græcia" di Catanzaro, 88100 Catanzaro, Italy

[4]NanoImaging Core Facility, Centre de Resources et Recherches Technologiques, Institut Pasteur, 75015 Paris, France

[5]Molecular Microbiology and Structural Biochemistry Laboratory, CNRS UMR 5086, University of Lyon, 69367 Lyon, France

[6]Department of Biochemistry & Molecular Biology, Indiana University School of Medicine, Indianapolis, IN 46202, USA

[7]School of Chemistry, Cardiff University, Park Place, Cardiff CF10 3AT, UK

[8]Foundation for Applied Molecular Evolution, Alachua, FL 32615, USA

[9]Present address: Dipartimento di Scienze Biomolecolari, Università degli Studi di Urbino "Carlo Bo", 61029 Urbino, Italy

[10]Present address: Dipartimento di Scienze della vita e dell'ambiente, Università degli Studi di Cagliari, 09042 Cagliari, Italy

[*]Co-corresponding author

ABSTRACT

How motions in enzymes might be linked to catalytic function is of considerable general interest. Recent advances in X-ray crystallography and cryogenic electron microscopy offer the promise of elucidating functionally relevant motions in proteins that are not easily amenable to study by other biophysical methods. Here we use 3D variability analysis (3DVA) on cryo-EM maps for wild type (WT) human asparagine synthetase (ASNS) and the R142I ASNS variant to identify conformational changes in the Arg-142 side chain, which mediates the formation of a catalytically relevant intramolecular tunnel. Our 3DVA results for WT ASNS are consistent with independent molecular dynamics (MD) simulations on a model generated from the X-ray structure of human ASNS. Moreover, MD simulations of computational models for the ASNS/β-aspartyl-AMP/$MgPP_i$ and R142I/β-aspartyl-AMP/$MgPP_i$ ternary complexes, suggest that the structural integrity of the tunnel is impaired in the R142I variant when β-aspartyl-AMP is present in the synthetase active site. The kinetic properties of the R142I ASNS variant support the proposed function of Arg-142. These studies illustrate the power of cryo-EM to identify localized motions and dissect the conformational landscape of large proteins. When combined with MD simulations, 3DVA is a powerful approach to understanding how conformational dynamics might regulate function in multi-domain enzymes possessing multiple active sites.

There is considerable general interest in understanding how enzyme motions might be linked to function[1-5], although their precise contribution to catalysis remains the subject of debate[6,7]. Certainly, allosteric regulation of enzyme activity depends on correlated residue movements[8,9], and computer-based simulations[10,11] support the idea that altered dynamics can be correlated with improvements in the catalytic efficiency of "designer" enzymes as they undergo optimization by directed evolution[12,13]. Equally, hydrogen-deuterium exchange (HDX) experiments suggest that local motions in a distal, solvent-exposed loop of soybean lipoxygenase are correlated with C-H activation energy barriers in the active site[14,15]. Dynamical motions have also been shown to mediate rapid interconversion of thermally accessible conformational states in enzymes, although many of these states are not catalytically competent[16]. Substrate binding biases the conformational ensemble of the free enzyme to favor structures in which reaction can take place[17,18]. These ideas have mostly been developed, however, from NMR studies on enzymes that possess only a single active site. Much less is known about how dynamical motions impact catalysis in enzymes that possess two, or more, active sites, such as glutamine-dependent amidotransferases[19-21] or tryptophan synthase[22]. Such multi-site enzymes are widely regarded as being too large for routine NMR-based studies of their motions in solution[23]. We note, however, that chemical shift perturbations have been used to elucidate the molecular basis of allosteric activation in the heterodimeric complex of imidazole glycerol phosphate synthase[24]. In addition, methyl-transverse relaxation-optimized spectroscopy (TROSY)[25] has the potential to obtain dynamical information for large, multi-site enzymes if isotopically labeled methyl groups in valine, isoleucine or leucine residues can be introduced into the protein[26,27].

The past decade has seen rapid advances in new experimental techniques for observing the structural dynamics of proteins[3,28-30]. In addition, computational methods to analyze EM-derived maps[31] are providing new opportunities to obtain information on the dynamical motions of enzymes directly from the map density[32,33]. How these motions are affected by external conditions, including buffer pH and concentration, ligand binding and temperature[34],

can therefore now (in principle) be examined. Here, we use human ASNS, a Class II glutamine-dependent amidotransferase that mediates asparagine biosynthesis[35,36], as a model system to evaluate whether EM-derived maps can provide any insights into the conformational changes that mediate function in a multi-site enzyme.

Human ASNS is of considerable biomedical interest, having been linked to metastatic progression in breast cancer[37], sarcoma cell proliferation[38], and decreased effectiveness of clinical treatments for acute lymphoblastic leukemia[39]. ASNS variants are also strongly correlated with impaired neural development in children[40], pointing to the importance of gaining an in-depth understanding of catalytic mechanism and regulation of the enzyme. Structural[41,42] and biochemical studies show that ASNS is built from two domains, each of which contains an active site that catalyzes one of the “half-reactions” needed for the overall conversion of aspartate to asparagine (Supplementary Fig. S1)[43-45]. As in all other glutamine-dependent enzymes, catalytic turnover requires that ammonia must be transported between the two active sites through the intramolecular tunnel[46,47].

We find that combining the analysis of EM-derived structures[48] with atomistic MD simulations[49,50] reveals that a single residue, Arg-142, mediates interconversion of the open and closed forms of the tunnel in human ASNS. This conclusion is bolstered by the EM structure and MD simulations of the R142I ASNS variant, in which Arg-142 is replaced by an isoleucine (the cognate residue in the bacterial homolog AS-B), and steady-state kinetic measurements. Our analysis also provides the first molecular understanding of how ligand binding in the synthetase active site might impact catalytic turnover by stabilizing the open form of the tunnel. This mechanism of regulating ammonia transfer in ASNS differs sharply from those operating in other Class II glutamine-dependent amidotransferases, which depend on large substrate-induced conformational rearrangements in their catalytic domains to form an intramolecular tunnel connecting the active sites[51,52].

RESULTS

Structure determination of human ASNS by cryo-EM.

Human ASNS was expressed in insect cells and purified as described previously[53,54], except that purification was performed under reducing conditions to preserve a native state of the enzyme (see Methods). Single-particle images of unmodified, recombinant human ASNS (apo-ASNS) were collected and processed using cryoSPARC.[55] To test the native state of ASNS in an unbiased fashion, the "blob particle picker" option of cryoSPARC was used to select ~1.2 million particles followed by several rounds of 2D classification as well as *ab initio* reconstructions, giving a final total of 12 initial reconstructions (Supplementary Fig. S2). Eleven of these reconstructions exhibited small densities (Supplementary Fig. S2d), which were further processed because they might correspond to a monomeric form of the enzyme (Supplementary Fig. S2f). We were not, however, able to converge these into a high-resolution map corresponding to the ASNS monomer. The twelfth reconstruction clearly resembled the "head-to-head" ASNS dimer seen in the X-ray crystal structure (Supplementary Figs. S2d and S3a)[41]. No initial 3D reconstruction resembling the "head-to-tail" dimer (Supplementary Fig. S3b) seen in the X-ray structure of the bacterial homolog (AS-B)[42] was found. We also examined the use of template-based particle picking with the AS-B dimer as template, but this attempt merely picked up a large number of junk particles (Supplementary Fig. S4). It is, therefore, unlikely that particles resembling AS-B exist; indeed, 3D reconstructions of particles selected in this study gave what appears to be a monomeric form of human ASNS (Supplementary Fig. S4). Taken together, these findings are consistent with human ASNS forming a "head-to-head" rather than a "head-to-tail" dimer. Realizing that the EM map of ASNS was similar to the crystal structure (Supplementary Figs. S2d and S3a), we used a template-based particle picking strategy to pick good particles efficiently. Data processing (see Methods) eventually gave rise to a map with 3.5 Å overall resolution (Supplementary Figs. S2, and S5-S7, Table S1). The model derived from EM map (Fig. 1) was generated by utilizing our previous crystal structure of DON-modified human ASNS (PDB: 6GQ3)[41].

Our new EM structure answers several questions concerning the validity of the high-resolution X-ray crystal structure of human ASNS[41] in which the Cys-1 side chain is modified by treatment with 6-diazo-5-oxo-L-norleucine (DON)[56]. First, two monomers of unmodified human ASNS in the native state form a “head-to-head” dimer as a result of intermolecular interactions involving residues 31-34 in the adjacent N-terminal domains. The antiparallel orientation of these two peptide segments places the side chains of Arg-32 and Glu-34 (monomer A) so that they can form salt bridges with Glu-34 and Arg-32 (monomer B), respectively (Fig. 1d and Supplementary Fig. S8). Moreover, Phe-31 and Phe-33 in both monomers form a hydrophobic cluster on the other face of the dimerization motif that likely contributes to the stability of the dimer interface in water. These contacts between the N-terminal domains of the ASNS monomers are almost identical to those observed in the X-ray structure. This is an important finding because the ASNS dimer seen by X-ray crystallography contains a disulfide bond that is unlikely to be present in the reducing environment of the cell[41]. We conclude that “head-to-head” dimerization is an intrinsic property of the mammalian enzyme, in contrast to the “head-to-tail” dimerization observed for AS-B by X-ray crystallography (Supplementary Fig. S3)[42]. Second, the EM and X-ray structures of human ASNS both lack density for residues in two loop segments (residues 201-220 and residues 465-475) and the C-terminal tail (residues 539-560 and 536-560 in the EM and X-ray structures, respectively) (Supplementary Fig. S9). Given that the apo-ASNS used to obtain the EM structure was prepared under physiologically relevant conditions, it is likely that these regions are disordered rather than being absent due to proteolysis as we originally speculated[41]. In addition, SDS-PAGE characterization of the human ASNS samples used in these cryo-EM studies shows no evidence for the presence of enzyme fragments (Supplementary Fig. S10).

Finally, amino acid side chains pointing into the tunnel (Val-119, Val-141, Arg-142, Leu-255, Met-344, Ala-404 and Leu-415) are also clearly evident in the EM structure (Fig. 2a). These side chains are predominantly hydrophobic, consistent with the idea that ammonia is

translocated between the active sites in its neutral form. The presence of a polar side chain close to glutaminase site is interesting, especially because this residue, Arg-142, is conserved in mammalian asparagine synthetases (Supplementary Fig. 11). Ser-362 and Glu-364, which are both located in the part of the tunnel adjacent to the synthetase active site, are also conserved residues (Supplementary Fig. S11). As observed for the X-ray structure of DON-modified human ASNS, the intramolecular tunnel in the EM structure adopts a "closed", or discontinuous, form through which ammonia cannot diffuse (Fig. 2b and Supplementary Fig. S12). In contrast, the intramolecular tunnel is continuous when glutamine and AMP are bound within the active sites of the C1A AS-B variant (i.e., it is in an "open" form) (Supplementary Fig. S13)[42]. Given that the covalent modification of Cys-1 does not lead to stabilization of the "open" form of the tunnel, these observations are consistent with previous proposals that AMP binding is critical to permitting ammonia translocation[42,57].

Extracting dynamical information from the EM map of human ASNS

Competition experiments show that ammonia released from glutamine is not released into solution during asparagine synthesis and must therefore travel along the intramolecular tunnel[47]. This translocation cannot take place when the tunnel is "closed", as seen in the EM and X-ray structures of recombinant human ASNS, suggesting that gating of the tunnel is regulated by dynamical effects. To investigate whether such motions are present in the free enzyme, we applied 3D variability analysis (3DVA)[58,59] to the EM map of apo-ASNS. As detailed elsewhere[58], local vibrations in the protein structure are preserved by fast freezing, thereby leading to particles in which the enzyme may be captured in slightly different conformational states, if any exist. As a result, 3DVA can identify protein motions based on the variance of particle stacks to a volume along a principal component (PC) axis (see Supplementary Figs. S12 and S14). Analyzing the map of apo-ASNS along five PCs allowed us to convert the ensemble of EM densities into 100 high-resolution model structures (20 for each component), which showed side chain movements in the ammonia tunnel. We were therefore able to understand movements in apo-ASNS at high-resolution (Fig. 3) despite these

being smaller than those of larger proteins, such as multidrug ABC exporters[60]. Although no change is seen in two PCs (components 0 and 2) (Figs. 3b and 3d), the Arg-142 side chain is re-positioned in two other PCs to yield an “open” form of the tunnel (components 2 and 3) (Figs. 3c and 3e). This side chain, however, shows only a slight re-positioning in the fifth PC (component 4 in Fig. 3f). The simplest interpretation of these results is that interconversion of the “open” and “closed” forms of the tunnel can take place in the absence of bound ligands in the C-terminal synthetase domain.

MD simulations of the full-length apo-ASNS monomer

In light of prior work by Schulten[61-63] and Tama[64,65], which showed the utility of MD simulations for interpreting cryo-EM maps, we turned to computer-based approaches[66,67] to test the conclusions from our 3DVA studies. Although a variety of computational strategies have been used to study conformational changes and the energetics of ammonia translocation in glutamine-dependent amidotransferases[68-73], these are the first such calculations for ASNS. Using the Robetta server[74], we constructed a model of full-length human apo-ASNS (Supplementary Fig. S15), containing the loops and residues 536-560 in the disordered tail that are not observed in the X-ray structure of the DON-modified human enzyme[41]. The resulting model, which was independent of the cryo-EM structure, was placed in a box of explicit water molecules and subjected to 200 ns of simulation at 298.15 K (see Methods). The tunnel in structures sampled during the trajectory was mapped using the algorithm implemented in the CAVER 3.0 software package.[75] In the initial (t = 20 ns) structure, access to the tunnel from the glutaminase active site is blocked by the side chains of Arg-142 and Leu-415. This “closed” form of the tunnel persisted for over 80 ns of simulation in apo-ASNS but underwent conversion into an ”open” form by 140 ns into the trajectory (Fig. 4a). Similar results were obtained in four replicate simulations of the apo-ASNS monomer (Supplementary Fig. S16), confirming the reproducibility of tunnel opening under our simulation conditions. We also determined that the tunnel undergoes multiple interconversions between the open and

closed forms in a microsecond MD trajectory, thereby establishing that the conformational preference of the Arg-142 side chain was not biased by sampling or the force field (Supplementary Fig. S17a). Finally, we showed that these conformational outcomes were unaltered in an MD trajectory of the human apo-ASNS dimer under identical simulation conditions. No significant differences in the fluctuations of either monomer in the dimer were observed when these monomers were compared to each other or to the isolated apo-ASNS monomer used in the studies of tunnel opening outlined above (Supplementary Fig. S18).

A detailed analysis of the structural snapshots taken throughout the replicate trajectories of the apo-ASNS monomer reveals that tunnel opening is a consequence of a 90° reorientation of the Arg-142 side chain, consistent with our EM-based conclusions (Figs. 3c and 3e). The new orientation of Arg-142 is stabilized by a salt bridge with the Asp-405 side chain (t = 200 ns); the latter residue is located at the interface between the two domains of the enzyme, providing a molecular basis for the coordination of tunnel opening with changes in domain-domain interactions. Forming the Arg-142/Asp-405 salt bridge requires breaking a network of intramolecular interactions, involving Arg-142, Glu-414, Arg-415 and Asn-75, that is present in the initial (t = 0 ns) structure. Given that the Asn-75 side chain forms the oxyanion hole required for glutamine hydrolysis[76], breaking this network provides a potential molecular mechanism by which tunnel opening might be coordinated with ammonia release in the glutaminase active site. Remarkably, the open form of the tunnel computed for the apo-ASNS monomer, in the absence of ligands in the N- and C-terminal active sites, is not dissimilar to that seen in the X-ray crystal structure of the bacterial C1A/glutamine/AMP ternary complex (Supplementary Fig. S19).

In order to assess the extent to which these MD simulations of the apo-ASNS monomer were consistent with experiment, the root mean square fluctuations (RMSF) of backbone heavy atoms in all 100 of the 3DVA-derived EM structures were calculated using CPPTRAJ[77] and compared with those computed from structures sampled in the replicated MD trajectories.

RMSF values were normalized to the largest value in each dataset before being used in this comparison, with the goal of offsetting differences in the magnitude of movements seen in the MD simulations and those based on the restrained coordinates used to construct the EM map (Fig. 5a). This comparison confirms that the motions revealed by 3DVA correspond to those seen in the MD simulation. We note that the small number of residues exhibiting significant differences in the comparison are those adjacent to missing segments in the EM structure. Equally, the large fluctuations of the C-terminal tail in the replicated MD trajectories are almost certainly a consequence of these residues being mis-positioned in the initial model (t = 0 ns). This level of agreement between experiment and theory strongly supports the EM-derived mechanism in which movement of the Arg-142 side chain results in tunnel opening and ammonia translocation.

MD simulations of the full-length apo-R142I ASNS variant monomer

As noted above, Arg-142, is conserved in mammalian asparagine synthetases. Sequence and structural alignments, however, show that this residue is isoleucine (Ile-143) in *Escherichia coli* AS-B even though nearby residues are conserved in both homologs (Supplementary Fig. 11).[41] We therefore used MD simulations to investigate the effects of replacing the polar arginine by a non-polar isoleucine on tunnel structure. The initial model of the full-length monomer of the apo-R142I ASNS variant was built from the energy minimized model of apo-ASNS described above. Following identical procedures to those used for apo-ASNS, we observed that the tunnel remained open over the course of the MD simulations (Fig. 4b). In part, this behavior may merely be a consequence of the reduced size of the Ile-142 side chain, although distance measurements throughout the four replicate MD simulations showed that the Ile-142 side chain underwent far less movement, perhaps to avoid forming interactions with the polar carboxylate groups of Asp-405 and Glu-414 (Supplementary Fig. S20). Comparing the RMSF values for residues in the R142I ASNS variant with the WT enzyme

showed that the presence of the isoleucine side chain has a relatively small impact on the overall dynamics of the apo-enzyme (Supplementary Fig. S20a).

Structure determination of the human R142I ASNS variant by cryo-EM.

We evaluated the predictions of these MD simulations by determining the structure of the R142I variant dimer at 3.35 Å resolution by cryo-EM (Supplementary Table S1 and Supplementary Figs. S21-S24). As expected, replacing a polar group by a hydrophobic side chain had little impact on the overall structure of the enzyme (0.483 Å RMSD of WT vs. the R142I variant; Supplementary Fig. S22), although it did give rise to structural changes in the tunnel region. Indeed, the tunnel linking the two active sites was now observed to be open, similar to that observed for AS-B (Supplementary Fig. S25), as was the case in the MD simulations. 3D variability analysis of the EM map of the R142I variant showed that the Ile-142 side chain adopts only a single conformation (Supplementary Fig. S26). Indeed, this single amino acid substitution appears to rigidify the entire protein, as indicated by a 2-fold reduction in the observed particle distribution in the 3DVA (compare Supplementary Figs. S14 and S27).

MD simulations of the human ASNS/β-aspartyl-AMP/$MgPP_i$ and the R142I/β-aspartyl-AMP/$MgPP_i$ ternary complexes.

Given the possibility that perturbations to the structural and dynamical properties of the tunnel might take place in the presence of bound intermediates, we investigated how ligand binding at the C-terminal synthetase domain might impact the conformational preferences of tunnel residues. Our initial calculations employed a model of the human ASNS/β-aspartyl-AMP/$MgPP_i$ ternary complex that was built by docking the ligands β-aspartyl-AMP and $MgPP_i$ into the model of WT apo-ASNS used in the MD simulations discussed above (see Methods and Supplementary Fig. S15b). Under identical simulation conditions to those used for apo-ASNS, and despite being in the “closed” form in the initial (t = 0 ns) structure, the tunnel

converted into a continuous, open form within 80 ns (Fig. 6a, and Supplementary Figs. S16b and S28). A detailed analysis of the trajectory for this ternary complex showed that the presence of β-aspartyl-AMP in the synthetase site disrupts the network of salt bridges involving Arg-142 due to an interaction between the Arg-403 side chain and the carboxylate in the intermediate (Supplementary Fig. S29). As a result, Asp-405 undergoes a conformational change that stabilizes the "tunnel open" orientation of the Arg-142 side chain (Fig. 6c). These findings were confirmed in replicate simulations (Supplementary Fig. S28). As for apo-ASNS, we also confirmed that the tunnel undergoes multiple interconversions between the open and closed forms in a microsecond MD trajectory of the human ASNS/β-aspartyl-AMP/$MgPP_i$ ternary complex (Supplementary Fig. S16b).

Replacing Arg-142 in the initial (t = 0 ns) structure of the human ASNS/β-aspartyl-AMP/$MgPP_i$ ternary complex by isoleucine gave a model of the cognate R142I ternary complex, which was then used in MD simulations under conditions identical to those used for the WT ternary complex (Supplementary Fig. S30). Unexpectedly, the presence of ligands in the synthetase active site significantly perturbed the structural properties of the tunnel in the R142I ternary complex (Fig. 6b and Supplementary Fig. S30). Thus, the tunnel appeared to be discontinuous in the trajectory snapshots taken at 20, 80 and 140 ns even though it was open in the initial (t = 0 ns) structure. Thus, the persistence of a closed tunnel conformation will likely preclude ammonia translocation between the active sites despite the tunnel close to Ile-142 being open. An additional branch seen in the final trajectory snapshot (t = 200 ns) may also ultimately provide a conduit by which ammonia can leak from the glutaminase site into bulk solution. Whatever the true molecular picture, it is clear that the structural integrity of the tunnel is impaired in the absence of Arg-142 and the presence of the β-aspartyl-AMP intermediate.

Steady-State Kinetic Measurements

As stated above, our EM structure and MD simulations suggest that replacing Arg-142 by isoleucine results in tunnel gate opening and rigidification of the ASNS variant in the absence of ligands. Yet, unexpectedly, closed and/or abnormal tunnel structures are observed in the MD trajectory of the R142I/β-aspartyl-AMP/$MgPP_i$ ternary complex, implying a change in function even though all catalytically important residues in either of the two active sites are unaltered.

Steady-state kinetic assays were therefore performed to test this computational prediction, and to determine the functional effects of replacing Arg-142 by isoleucine. In these experiments, the MgATP concentration was fixed, and activity was measured by detecting the formation of inorganic pyrophosphate (PP_i) production[78], which is formed in a 1:1 stoichiometry with L-asparagine by WT ASNS[57]. We also investigated the activity of the R142A ASNS variant, in which Arg-142 is replaced by alanine. This variant was chosen because the alanine side chain is small. As a result, the tunnel should adopt an open conformation in this variant because Ala-142 is unable to form intramolecular interactions with other residues in the enzyme. When ammonia was used as the nitrogen source, varying the L-aspartate concentration gave steady-state parameters for the two variants that were essentially unchanged compared to those of WT ASNS (Table 1 and Supplementary Fig. S31). Equally, when L-aspartate was varied at saturating levels of L-glutamine, but in the absence of ammonia, the kinetics of PPi formation were only mildly affected, with 4- and 2-fold reductions in turnover number being observed for the R142I and R142A variants, respectively. In contrast, varying L-glutamine concentrations at saturating concentrations of L-aspartate, gave 8- and 5-fold reductions in turnover number for the R142I and R142A ASNS variants, respectively, even though a substantial decrease in $^{app}K_M$ for L-glutamine is observed.

At first sight, given that the tunnels in the two variants are in an open conformation (as seen in both MD simulations and the cryo-EM structure of the unliganded R142I variant) one might expect no impact on catalytic activity under our assay conditions because ammonia translocation is unlikely to be the rate-limiting step in the catalytic cycle. Replacing the positively charged Arg-142 side chain by smaller, hydrophobic groups, however, clearly alters how the C-terminal synthetase domain in human ASNS responds to different nitrogen sources. This finding is consistent with impaired ammonia transport through the tunnel, as implied in our MD simulations of the ASNS/β-aspartyl-AMP/$MgPP_i$ ternary complex. Equally, and as observed in similar studies of carbamoyl phosphate synthetase[79], the structure and/or dynamics of the tunnel in the R142I variant may be altered in the presence of the β-aspartyl-AMP intermediate so that ammonia, produced in the N-terminal active site, can leak directly into bulk solution. Whatever the molecular basis for the altered steady-state kinetic parameters of the two ASNS variants, however, these kinetic studies support the hypothesis that Arg-142 is important for tunnel function, L-glutamine recognition, and the structural integrity of the tunnel given that free ammonia likely accesses the synthetase site directly rather than passing through the intramolecular tunnel.

DISCUSSION

The successful determination of a cryo-EM structure for human ASNS establishes the physiologically relevant form of the human ASNS dimer and provides a basis for understanding how cytotoxic ASNS inhibitors, which are potential anti-cancer agents[80], might interact with the enzyme[81]. More generally, our findings demonstrate the utility of cryo-EM in providing information on protein motions[82], even at the level of a single residue in an enzyme possessing multiple active sites. Arg-142 functions as a “gate” that interconverts the open and closed forms of the tunnel; it also maintains the structural integrity of the tunnel when /β-aspartyl-AMP and MgPPi are present in the C-terminal active site. This gating mechanism contrasts sharply with structural observations on other Class II amidotransferases for which

substrate binding initiates large conformational rearrangements that lead to tunnel formation and activation of glutaminase activity[83]. For example, the presence of 5'-phosphoribosyl-1'-pyrophosphate (PRPP) in the C-terminal active site is required to produce the open form of the intramolecular tunnel in *Escherichia coli* PRPP amidotransferase (Supplementary Fig. S32a)[51]. MD simulations have confirmed that PRPP binding stabilizes the conformation of a key active site loop, which is disordered in the free enzyme[84]. A large-scale rearrangement of the C-terminal tail in glutamine fructose-6-phosphate amidotransferase (GFAT) is also observed when fructose-6-phosphate binds to the synthetase site in the C-terminal domain of the enzyme[52], leading to sequestration of the substrate from water and ammonia tunnel formation. Generating a continuous, open tunnel in GFAT, however, requires reorientation of the two domains and rotation of the Trp-74 side chain, a structure that is unlikely to be adopted by the free enzyme (Supplementary Fig. S32b)[85].

MD simulations provide evidence that the "open" form of the intramolecular tunnel might be energetically favored by the formation of β-aspartyl-AMP in the C-terminal domain of the enzyme. More importantly, they reveal the importance of Arg-142 in maintaining the structural integrity of the tunnel before this reaction intermediate undergoes reaction with ammonia; a finding that seems to be supported by the kinetic properties of the R142I variant (Table 1). Indeed, it seems that catalytic events in the C-terminal active site impact Arg-142, located at a distance of approximately 20 Å in the glutaminase domain, due to motions within a network of salt bridges. Catalytic turnover in glutamine-dependent ASNS activity therefore depends on residues defining the tunnel connecting the active sites, as well as those directly involved in catalysis and the stabilization of reactive intermediates. Our results provide an example of how global regulatory mechanisms are embedded within the protein scaffold far away from the active site(s) and emphasize the need to consider the total conformational ensemble of proteins in efforts to obtain enzymes by *de novo* computational design[86].

METHODS

Protein expression and purification.

The expression and purification of WT human ASNS was carried out as described previously[53], except that 5 mM β-mercaptoethanol was present in all buffers used during protein purification. Using a spin column, the recombinant enzyme was concentrated to 9 mg/mL in 25 mM Tris-HCl, pH 8.0, containing 200 mM NaCl and 5 mM DTT. In the case of the two tunnel variants, R142A and R142I, cell pellets were sonicated for 4 minutes in lysis buffer containing 100 mM EPPS, pH 8, containing 300 mM NaCl, 50 mM imidazole, and 5 mM TCEP. After centrifugation at 12,000 rpm for 30 minutes at 4°C, the supernatant was loaded onto a Ni-NTA column equilibrated with the same buffer at 4°C. Each protein was eluted with 100 mM EPPS, pH 8, containing 300 mM NaCl, 250 mM imidazole, and 5 mM TECP. Fractions containing protein were collected, and exchanged into 100 mM EPPS, pH 8, containing 150 mM NaCl, and 5 mM TCEP, using a PD-10 size exclusion column. The purified enzyme was concentrated using a spin filter, and its concentration was determined by Bradford assay. Aliquoted ASNS variant samples were stored at –80°C. For cryo-EM work, the sample buffer containing the ASNS R142I variant was exchanged to 25 mM Tris-HCl, pH 8.0, containing 200 mM NaCl and 5 mM DTT by dialysis. The dialysate was concentrated by a spin column to 3.2 mg/mL.

Cryo-EM sample preparation and data collection.

300 mesh UltrAuFoil R1.2/1.3 grids were glow-discharged for 1 minute with a current of 15mA in a PELCO easiGlow system before being mounted onto a Mark IV Vitrobot (FEI/Thermo Fisher Scientific). The sample chamber on the Vitrobot was kept at 4 °C with a relative humidity of 100%. A 3.0 µL sample of either recombinant WT ASNS or the R142I variant, at concentrations of 9.0 mg/mL and 3.2 mg/mL, respectively, was applied to the grid, which was then blotted from both sides for 4 s with the blot force set at 0. After blotting, the grid was rapidly plunge-frozen into a liquid ethane bath cooled by liquid nitrogen.

Single particle data was collected by a 200 kV Glacios transmission electron microscope (FEI/ThermoFisher Scientific) equipped with a Falcon4 camera operated in Electron-Event Representation (EER) mode[87]. Movies were collected using EPU at 150,000x magnification (physical pixel size 0.93 Å) over a defocus range of −0.4 to −2.0 µm and a total accumulated dose of 40 e/ $Å^2$. Camera gain reference was taken at the end of the run. A total of 3,584 movies were acquired for WT ASNS and 4,101 movies for R142I variant. Data were processed using cryoSPARC v3.2.2 and v4.4.1 over the duration of the project. Each movie was split into 40 fractions during motion correction with an EER upsampling factor of 1. After motion correction and CTF estimation, micrographs were manually curated based on relative ice thickness and CTF resolution fit such that 2,103 micrographs out of corresponding 3,584 movies for WT and 2,649 out of 4,101 movies for the R142I variant were chosen and used for subsequent data processing.

Assessing the mode of ASNS dimerization and structure determination.

To gauge how ASNS dimerizes in an unbiased fashion, particles were initially selected using the "blob pick" option in cryoSPARC[55]. 2D class averages showed what appeared to be 2D projections of a human ASNS dimer similar to that seen in the X-ray structure[41] (Supplementary Fig. S2b). Further, 769,800 particles were subjected to two rounds of *ab initio* reconstruction, resulting in a total of 12 initial reconstructions (Supplementary Fig. S2d). One reconstruction clearly resembles the head-to-head dimer form of ASNS (compare Supplementary Fig. S2d and S2e), and the rests exhibited small densities. In light of this observation, particle selection was then carried out by template-based picking, using a template generated from the X-ray structure (PDB: 6GQ3) in UCSF Chimera[88]. The full cryo-EM data processing workflow of WT ASNS is illustrated in Supplementary Fig S3. Bad particles were removed using several rounds of 2D classification followed by 5 rounds of *ab initio* reconstructions, and successive heterologous refinement, non-uniform refinement with

CTF and defocus correction, and the imposition of C_2 symmetry gave rise to a map with 3.5 Å overall resolution. The map was sharpened using the program DeepEMhancer[89] as implemented on the COSMIC[2] site[90]. Model building started with fitting the crystal structure (PDB: 6GQ3)[37] into the EM map using rigid body refinement by REFMAC[91]. The resulting model was then iteratively refined by real-space refinement in Phenix[92] followed by manual inspection and refinement in Coot[93]. Figures for the cryo-EM density maps and models were generated with Chimera[87] or ChimeraX[94]. The full cryo-EM data processing workflow of R142I variant is illustrated in Supplementary Fig S22. The data processing for ASNS R142I was carried out by a template-picking strategy. Bad particles were removed using several rounds of 2D classification followed by 5 rounds of *ab initio* reconstructions, and successive heterologous refinement, non-uniform refinement with CTF and defocus correction, and the imposition of C_2 symmetry gave rise to a map with 3.35 Å overall resolution. The map was sharpened using the program DeepEMhancer[89] as implemented on the COSMIC[2] site[90]. Model building for the R142I ASNS variant was carried out by essentially the same procedure as that described for WT ASNS except that the EM structure of the enzyme (PDB: 8SUE) was used as an initial model.

3D variability analysis (3DVA) of the EM map for human ASNS.

Each EM map of WT ASNS and the R142I variant was separately subjected to 3D variability analysis (3DVA) in cryoSPARC v4.4.1 filtered at 4 Å resolution with the mask previously used in a final non-uniform refinement[55]. Five principal components were used in both analyses. A movie for each component (Supplementary Movies M1-M5 for WT ASNS, Supplementary Movies M6-M10 for the R142I variant) was made with UCSF Chimera[88] using frames generated by the 3DVA display program in a simple mode in cryoSPARC v4.4.1. Movie frames were subjected to variability refinement in Phenix, using 50 models per map, yielding a series of 20 models per component. Backbone RMS fluctuations for each residue in the set of 100 structures obtained for WT ASNS were then computed using the CPPTRAJ software package[77].

Molecular dynamics simulations.

The Robetta server[74] was used to build a model of **full-length** human WT ASNS in order to add the residues that were not observed in the X-ray structure. In addition, this structure contained an unmodified side chain for Cys-1. The protonation state of ionizable residues at pH 7.4 was determined by calculation using the PROPKA algorithm[95], as implemented in Maestro (Schrodinger Suite 2018-01) (Supplementary Table S2).

A model of the human ASNS/β-aspartyl-AMP/$MgPP_i$ ternary complex was then obtained by positioning the Mg(II) salt of inorganic pyrophosphate (PPi) into the initial WT apo-ASNS model such that MgPPi was in an identical location to that observed in GMP synthetase[96] and other members of the PP-loop ATP pyrophosphatase superfamily[97]. β-aspartyl-AMP was docked into the model of the binary complex so that the nucleobase was in a similar site to that seen for AMP in the X-ray crystal structure of the bacterial enzyme[42]. The protonation state of ionizable groups in the protein and the two ligands were assigned using PROPKA[95] and Epik[98], respectively. As a result, the amino and carboxylate groups of the aspartate-derived portion of β-aspartyl-AMP formed complementary electrostatic and hydrogen bonding interactions with Gly-365, Asp-367, Glu-368 and Arg-403 (Supplementary Fig. S11 and Supplementary Table S2). These four residues are conserved in known glutamine-dependent asparagine synthetases (Supplementary Fig. S11).

Each of these models was energy minimized before being placed in a box of TIP3P water molecules[99], which was sized to ensure a minimum distance of 10 Å between protein atoms and the sides of the box. After the addition of sodium ions to neutralize the total charge of the system, each model was heated to 300 K and equilibrated in the NPT ensemble (P = 101,325 Pa). Four 200 ns NPT MD simulations for each of these two models were then carried out, with the OPLS_2005 force field[100] parameters describing the protein and the β-aspartyl-AMP intermediate. In a control simulation, a microsecond trajectory was computed for the apo-

ASNS monomer under identical conditions. These calculations were performed using the DESMOND MD package (D.E. Shaw Research, New York, NY, 2018). Snapshots were taken at 200 ps intervals in MD simulations of the trajectories for WT ASNS and the WT ASNS/β-aspartyl-AMP/$MgPP_i$ ternary complex (Supplementary Movies M11 and M12, respectively).

A computational model of the WT ASNS dimer was built by superimposing two copies of the initial apo-ASNS monomer model on the X-ray crystal structure of human ASNS.[41] As outlined above for the MD simulations of the apo-ASNS monomer, the resulting dimer was energy minimized, placed in a box of explicit TIP3P water molecules, and heated/equilibrated to 300 K. A 200 ns NPT MD simulation of the resulting system was then carried out, with the OPLS_2005 force field[100] parameters describing the protein. Snapshots were taken at 200 ps intervals in MD simulations of the trajectory.

Finally, initial models of the apo-R142I ASNS variant and the R142I/β-aspartyl-AMP/$MgPP_i$ ternary complex were built by graphically replacing Arg-142 by isoleucine (Maestro GUI) in the initial, unoptimized models of the apo-ASNS and the ASNS/β-aspartyl-AMP/$MgPP_i$ ternary complex. These R142I-containing models were energy minimized and heated/equilibrated following identical procedures to those outlined above. Once again, four 200 ns NPT MD simulations were carried out with the DESMOND MD package using identical conditions to those outlined above for the WT enzyme and its ternary complex. Snapshots were taken at 200 ps intervals in MD simulations of the trajectories for the R142I variant and the R142I/β-aspartyl-AMP/$MgPP_i$ ternary complex (Supplementary Movies M13 and M14, respectively).

All MD simulations employed periodic boundary conditions (cubic box), and long-range electrostatic interactions were calculated by particle mesh Ewald[101] with short-range interactions being truncated at 9 Å. Trajectories were analyzed using CAVER 3.0 (default settings) to determine the conformation of the intramolecular tunnel in sampled protein

structures[75], and backbone RMS fluctuations for the structures in the four MD trajectories were computed using CPPTRAJ[77].

Steady-state kinetic measurements.

The rate of pyrophosphate production catalyzed by recombinant, WT human ASNS and two ammonia tunnel variants was determined in a continuous assay format using the EnzChek™ Pyrophosphate Assay Kit (Molecular Probes, Eugene, OR). Briefly, ASNS-catalyzed pyrophosphate production was measured at 37 °C over a 4-minute period by monitoring the absorption at 360 nm. In this assay, the reaction (400 μL) was initiated by the addition of enzyme (50 nM) to a reaction mixture containing 2-amino-6-mercapto-7-methylpurine ribonucleoside (0.2 mM), purine nucleoside phosphorylase (1 U/mL), inorganic phosphatase (0.09 U/mL), and substrates in 100 mM EPPS, pH 8, containing 2 mM dithiothreitol, 10 mM $MgCl_2$ and 5 mM ATP. When L-aspartate was varied (0-12.5 mM), the concentration of either L-glutamine (20 mM) or NH_4Cl (100 mM) was fixed. Similarly, when either glutamine (0-20 mM) or NH_4Cl (0-100 mM) was varied, the L-aspartate (10 mM) concentration was constant. Data analysis was performed using GraphPad Prism (GraphPad Holdings, La Jolla).

Data Availability

EM-derived structural data of WT human ASNS and the R142I ASNS variant have been deposited in the PDB (PDB ID: 8SUE and 9B6G, respectively) and in the Electron Microscopy Data Bank (EMDB ID: EMD-40764 and EMD-44253, respectively). Coordinate files for the 200 structures used in 3D variability analyses for WT human ASNS and the R142I ASNS variant, and the four MD-derived trajectories can be downloaded using links provided in the Supplementary Material.

REFERENCES

1. Schwartz, S. D. Protein dynamics and enzymatic catalysis. *J. Phys. Chem. B* **127**, 2649-2660 (2023)
2. Klinman, J. P. Dynamical activation of function in metalloenzymes. *FEBS Lett.* **597**, 79-91 (2023).
3. Xu, D., Meisburger, S. & Ando, N. Correlated motions in structural biology. *Biochemistry* **60**, 2331-2340 (2021).
4. Agarwal, P. K. A biophysical perspective on enzyme catalysis. *Biochemistry* **58**, 438-449 (2019).
5. Nashine, V. C., Hammes-Schiffer, S. & Benkovic, S. J. Coupled motions in enzyme catalysis. *Curr. Op. Chem. Biol*. **14**, 644-651 (2010).
6. Warshel, A. & Bora, R. P. Defining and quantifying the role of dynamics in enzyme catalysis. *J. Chem. Phys.* **144**, 180901 (2016).
7. Klinman, J. P., Offenbacher, A. R. & Hu, S. Origins of enzyme catalysis: Experimental findings for C-H activation, new models, and their relevance to prevailing theoretical constructs. *J. Am. Chem. Soc*. **139**, 18409-18427 (2017).
8. Guo, J. & Zhou, H.-X. Protein allostery and conformational dynamics. *Chem. Rev.* **116**, 6503-6515 (2016).
9. Offenbacher, A. R., Iavarone, A. T. & Klinman, J. P. Hydrogen-deuterium exchange reveals long-range dynamical allostery in soybean lipoxygenase. *J. Biol. Chem.* **293**, 1138-1148 (2018).
10. Bunzel, H. A., Anderson, J. L. R., Hilvert, D., Arcus, V. L., van der Kamp, M. W. & Mulholland, A. J. Evolution of dynamical networks enhances catalysis in a designer enzyme. *Nat. Chem.* **13**, 1017-1022 (2021).
11. Otten, R., Pádua, R. A. P., Bunzel, H. A., Nguyen, V., Pitsawong, W., Patterson, M., Sui, S., Perry, S. L., Cohen, A. E., Hilvert, D. & Kern, D. How directed evolution reshapes the energy landscape in an enzyme to boost catalysis. *Science* **370**, 1442-1446 (2020).

12. Joo, H., Lin, Z. & Arnold, F. H. Laboratory evolution of peroxide-mediated cytochrome P450 hydroxylation. *Nature* **399**, 670-673 (1999).

13. Wang, Y., Xue, P., Cao, M., Yu, T., Lane, S. T. & Zhou, H. Directed evolution: Methodologies and applications. *Chem. Rev.* **121**, 12384-12444 (2021).

14. Zaragoza, J. P. T., Offenbacher, A. R., Hu, S., Gee, C. L., Firestein, Z. M., Minnetian, N., Deng, Z., Fan, F., Iavarone, A. T. & Klinman, J. P. Temporal and spatial resolution of distal protein motions that activate hydrogen tunneling in soybean lipoxygenase. *Proc. Acad. Natl. Sci., USA* **120**, e2211630120 (2023).

15. Gao, S, & Klinman, J. P. Functional roles of enzyme dynamics in accelerating active site chemistry: Emerging techniques and changing concepts. *Curr. Op. Struct. Biol.* **75**, 102434 (2022).

16. Åqvist, J., Socan, J. & Purg, M. Hidden conformational states and strange temperature optima in enzyme catalysis. *Biochemistry* **59**, 3844-3855 (2022).

17. Henzler-Wildman, K. A., Lei, M., Thai, V., Kerns, S. J., Karplus, M. & Kern, D. A hierarchy of timescales in protein dynamics is linked to enzyme catalysis. *Nature* **450**, 913-917 (2007).

18. Eisenmesser, E. Z., Millet, O., Labeikovsky, W., Korzhnev, D. M., Wolf-Watz, M., Bosco, D. A., Skalicky, J. J., Kay, L. E. & Kern, D. Intrinsic dynamics of an enzyme underlies catalysis. *Nature* **438**, 117-121 (2005).

19. Zalkin, H. & Smith, J. L. Enzymes using glutamine as a nitrogen donor. *Adv. Enzymol. Relat. Areas Mol. Biol.* **72**, 87-144 (1998).

20. Huang, X., Holden, H. M. & Raushel, F. M. Channeling of substrates and intermediates in enzyme-catalyzed reactions. *Annu. Rev. Biochem.* **70**, 149-180 (2001).

21. Richards, N. G. J. et al. in *Comprehensive Natural Products II: Chemistry & Biology* Vol. 8 Ch. 6 (Elsevier, 2010).

22. Pan, P., Woehl, E. & Dunn, M. F. Protein architecture, dynamics and allostery in tryptophan synthase. *Trends Biochem. Sci.* **22**, 22-27 (1997).

23. Kovermann, M., Rogne, P. & Wolf-Watz, M. Protein dynamics and function from solution state NMR spectroscopy. *Q. Rev. Biophys.* **49**, e6 (2016).

24. Wurm, J. P., Sung, S., Kneuttinger, A. C., Hupfeld, E., Sterner, R., Wilmanns, M. & Sprangers, R. Molecular basis for the allosteric activation mechanism of the heterodimeric imidazole glycerol phosphate synthase complex. *Nat. Commun.* **12**, 2748 (2021).

25. Tugarinov, V., Hwang, P. M., Ollerenshaw, J. E. & Kay, L. E. Cross-correlation relaxation enhanced ^{1}H-^{13}C NMR spectroscopy of methyl groups in very high molecular weight proteins and protein complexes. *J. Am. Chem. Soc.* **125**, 10420-10428 (2003).

26. Overbeck, J. H., Stelzig, D., Fuchs, A.-L., Wurm, J. P. & Sprangers, R. Observation of conformational changes that underlie the catalytic cycle of Xrn2. *Nat. Chem. Biol.* **18**, 1152-1160 (2022).

27. Rosenzweig, R., Moradi, S., Zarrine-Asfar, A., Glover, J. R. & Kay, L. E. Unraveling the mechanism of protein disaggregation through a ClpB-DnaK interaction. *Science* **339**, 1080-1083 (2013).

28. Meisburger, S., Case, D. A. & Ando, N. Robust total X-ray scattering workflow to study correlated motions of proteins in crystals. *Nat. Commun.* **14**, 1228 (2023).

29. Thompson, M. C. et al. Temperature-jump solution X-ray scattering reveals distinct motions in a dynamic enzyme. *Nat. Chem.* **11**, 1058-1066 (2019).

30. Orville, A. M. Recent results in time resolved serial femtosecond crystallography at XFELs. *Curr. Op. Struct. Biol.* **65**, 193-208 (2020).

31. Beton, J. G., Cragnolini, T., Kaleel, M., Mulvaney, T., Sweeney, A. & Topf, M. Integrating model simulation tools and cryo-electron microscopy. *WIREs Comput. Mol. Sci.* **13**, e1642 (2023).

32. Vant, J. W., Sarkar, D., Nguyen, J., Baker, A. T., Vermaas, J. V. & Singharoy, A. Exploring cryo-electron microscopy with molecular dynamics. *Biochem. Soc. Trans.* **50**, 569-581 (2022).

33. Matsumoto, S., Ishida, S., Araki, M., Terayama, K. & Okuno, Y. Extraction of protein dynamics information from cryo-EM maps using deep learning. *Nat. Mach. Intel.* **3**, 153-160 (2021).

34. Tsai, M.-D., Wu, W.-J. & Ho, M.-C. Enzymology and dynamics by cryogenic electron microscopy. *Annu. Rev. Biophys.* **15**, 19-38 (2022)

35. Richards, N. G. J. & Schuster, S. M. Mechanistic issues in asparagine synthetase catalysis. Adv. Enzymol. *Relat. Areas Mol. Biol.* **72**, 145-198 (1998).

36. Lomelino, C., Andring, J. T., McKenna, R. & Kilberg, M. S. Asparagine synthetase: Function, structure, and role in disease. *J. Biol. Chem.* **292** 19952-19958 (2017).

37. Knott, S. R. V. et al. Asparagine bioavailability governs metastasis in a model of breast cancer. *Nature* **554**, 378-381 (2018).

38. Hettmer, S. et al. Functional genomic screening reveals asparagine dependence as a metabolic vulnerability in sarcoma. *eLife* **4**, e09436 (2015).

39. Jedraszek, K., Malczewska, M., Parysek-Wojcik, K. & Lejman, M. Resistance mechanisms in pediatric B-call acute lymphoblastic leukemia. *Int. J. Mol. Sci.* **23**, 3067 (2022).

40. Staklinski, S. J. et al. Cellular and molecular characterization of two novel asparagine synthetase gene mutations linked to asparagine synthetase deficiency. *J. Biol. Chem.* **298**, 102385 (2022).

41. Zhu, W. et al. High-resolution crystal structure of human asparagine synthetase enables analysis of inhibitor binding and selectivity. *Commun. Biol.* **2**, 345 (2019).

42. Larsen, T. M. et al. Three-dimensional structure of *Escherichia coli* asparagine synthetase B: A short journey from substrate to product. *Biochemistry* **38**, 16146-16157 (1999).

43. Boehlein, S. K., Richards, N. G. J. & Schuster, S. M. Glutamine-dependent nitrogen transfer in Escherichia coli asparagine synthetase B. *J. Biol. Chem.* **269**, 7450-7457 (1994).

44. Boehlein, S. K., Stewart, J. D., Walworth, E. S., Thirumoorthy, R., Richards, N. G. J. & Schuster, S. M. Kinetic mechanism of *Escherichia coli* asparagine synthetase B. *Biochemistry* **37**, 13230-13237 (1998).

45. Pfeiffer, N. E., Mehlhaff, P. M., Wylie, D. E. & Schuster, S. M. Topographical separation of the catalytic sites of asparagine synthetase explored with monoclonal antibodies. *J. Biol. Chem.* **262**, 11565-11570 (1987).

46. Richards, N. G. J., Humkey, R. N., Li, K., Meyer, M. E. & Sintjago de Cordova, T. C., in *Comprehensive Natural Products II: Chemistry & Biology* Vol. 8 Ch. 6 (Elsevier, 2010).

47. Li, K. K., Beeson, W. T., Ghiviriga, I. & Richards, N. G. J. A convenient gHMQC-based NMR assay for investigating ammonia channeling in glutamine-dependent amidotransferases: Studies of *Escherichia coli* asparagine synthetase. *Biochemistry* **46**, 4840-4849 (2007).

48. Wu, M. & Lander, G. C. Present and emerging methodologies in cryo-EM single-particle analysis. *Biophys. J.* **119**, 1281-1289 (2020).

49. Petrovic, D. & Kamerlin, S. C. L. Molecular modelling of conformational dynamics and its role in enzyme evolution. *Curr. Op. Struct. Biol.* **52**, 50-57 (2018).

50. Norberg, J. & Nilsson, L. Advances in biomolecular simulations: methodology and recent applications. *Q. Rev. Biophys.* **36**, 257-306 (2003).

51. Krahn, J. M., Kim, J. H., Burns, M. R., Parry, R. J., Zalkin, H. & Smith, J. L. Coupled formation of an amidotransferase ammonia tunnel and a phosphoribosyltransferase active site. *Biochemistry* **36**, 11061-11068 (1997).

52. Mouilleron, S., Badet-Denisot, M.-A. & Golinelli-Pimpaneau, B. Ordering of C-terminal loop and glutaminase domains of glucosamine-6-phosphate synthase promotes sugar ring opening and formation of the ammonia channel. *J. Mol. Biol.* **377**, 1174-1185 (2008).

53. Ciustea, M., Gutierrez, J. A., Abbatiello, S. E., Eyler, J. R. & Richards, N. G. J. Efficient expression, purification and characterization of C-terminally tagged, recombinant human asparagine synthetase. *Arch. Biochem. Biophys.* **440**, 18-27 (2005).

54. Imasaki, T., Wenzel, S., Yamada, K., Bryant, M. L. & Takagi, Y. Titer estimation for quality control (TEQC) method: A practical approach for optimal production of protein complexes using the baculovirus expression vector system. *PloS ONE* **13**, e0195356 (2018).

55. Punjani, A., Rubinstein, J. L., Fleet, D. J. & Brubaker, M. A. cryoSPARC: Algorithms for rapid unsupervised cryo-EM structure determination. *Nat. Methods* **14**, 290-296 (2017).

56. Jayaram, H. N., Cooney, D. A., Milman, H. A., Homan, E. R. & Rosenbluth, R. J. DON, CONV and DONV I. Inhibition of L-asparagine synthetase *in vitro*. *Biochem. Pharmacol.* **25**, 1571-1582 (1976).

57. Tesson, A. R., Soper, T. S., Ciustea, M. & Richards, N. G. J. Revisiting the steady state kinetic mechanism of glutamine-dependent asparagine synthetase from *Escherichia coli*. *Arch. Biochem. Biophys.* **413**, 23-31 (2003).

58. Afonine, P. V., Gobet, A., Moissonnier, L., Martin, J., Poon, B. K. & Chaptal, V. Conformational space exploration of cryo-EM structures by variability refinement. *Biochim. Biophys. Acta Biomembranes* **1865**, 184133 (2023).

59. Punjani, A. & Fleet, D. J. 3D variability analysis: Resolving continuous flexibility and discrete heterogeneity from single particle cryo-EM. *J. Struct. Biol.* **213**, 107702 (2021).

60. Chaptal, V. et al. Substrate-bound and substrate-free outward-facing structures of a multidrug ABC exporter. *Sci. Adv.* **8**, eabg9215 (2022).

61. Singharoy, A., Teo, I, McGreevy, R., stone, J. E., Zhao, J. & Molecular dynamics-based refinement and validation for sub-5 Å cryo-electron microscopy maps. *eLife* **5**, e16105 (2016).

62. Trabuco, L. G., Schreiner, E., Gumbart, J., Hsin, J., Villa, E. & Schulten, K. Applications of the molecular dynamics fitting method. *J. Struct. Biol.* **173**, 420-427 (2011).

63. Trabuco, L. G., Villa, E., Mitra, K., Frank, J. & Schulten, K. Flexible fitting of atomic structures into electron microscopy maps using molecular dynamics. *Structure* **16**, 673-683 (2008).

64. Miyashita, O., Kobayashi, C., Mori, T., Sugita, Y. & Tama, F. Flexible fitting to cryo-EM density map using ensemble molecular dynamics simulations. *J. Comput. Chem.* **38**, 1447-1461 (2017).

65. Orzechowski, M. & Tama, F. Flexible fitting of high-resolution X-ray structures into cryoelectron microscopy maps using biased molecular dynamics simulations. *Boiopgyss. J.* **95**, 5692-5705 (2008).

66. Costa, M. G. S., Gur, M., Krieger, J. M. & Bahar, I. Computational biophysics meets cryo-EM revolution in the search for the functional dynamics of biomolecular systems. *WIREs Comput. Mol. Sci.* **14**, e1689 (2024).

67. Vant, J. W., Sarkar, D., Nguyen, J., Baker, A. T., Vermass, J. V. & Singharoy, A. Exploring cryo-electron microscopy with molecular dynamics. *Biochem. Soc. Trans.* **50**, 569-581 (2022).

68. Sharma, N., Singh, S., Tanwar, A. S., Mondal, J. & Anand, R. Mechanism of coordinated gating and signal transduction in purine biosynthetic enzyme formylglycinamidine synthetase. *ACS Catalysis* **12**, 1930-1944 (2022).

69. Fan, Y., Lund, L., Yang, L., Raushel, F. M. & Gao, Y.-Q. Mechanism for transport of ammonia within carbamoyl phosphate synthetase determined by molecular dynamics simulations. *Biochemistry* **47**, 2935-2944 (2008).

70. Fan, Y., Lund, L., Shao, Q., Gao, Y.-Q. & Raushel, F. M. A combined theoretical and experimental study of the ammonia tunnel in carbamoyl phosphate synthetase. *J. Am. Chem. Soc.* **131**, 10211-10219 (2009).

71. Dewage, S. W. & Cisneros, G. A. Computational analysis of ammonia transfer along two intramolecular tunnels in *Staphylococcus aureus* glutamine-dependent amidotransferase (GatCAB). *J. Phys. Chem. B* **119**, 3669-3677 (2015).

72. Amaro, R., Myers, R. S., Davisson, V. J. & Luthey-Schulten, Z. A. Structural elements in IGP synthase exclude water to optimize ammonia transfer. *Biophys. J.* **89**, 475-487 (2005).

73. Wang, X. S., Roitberg, A. E. & Richards, N. G. J. Computational studies of ammonia channel function in glutamine 5'-phosphoribosylpyrophosphate amidotransferase. *Biochemistry* **48**, 12272-12282 (2009).

74. Kim, D. E., Chivian, D. & Baker, D. Protein structure prediction and analysis using the Robetta server. *Nucl. Acids Res.* **32**, W526-W531 (2004).

75. Chovancova, E. et al. CAVER 3.0: A tool for the analysis of transport pathways in dynamic protein structures. *PloS Comput. Biol.* **8**, e1002708 (2012).

76. Boehlein, S. K., Rosa-Rodriguez, J. G., Schuster, S. M. & Richards, N. G. J. Catalytic activity of the N-terminal domain of *Escherichia coli* asparagine synthetase B can be reengineered by single-point mutation. *J. Am. Chem. Soc.* **119**, 5785-5791 (1997).

77. Roe, D. R. & Cheatham, T. E., III. PTRAJ and CPPTRAJ: Software for processing and analysis of molecular dynamics trajectory data. *J. Chem. Theory Comput.* **9**, 3084-2095 (2013).

78. Upson, R. H.; Haugland, R. P.; Malekzadeh, M. N.; Haugland, R. P. A spectrophotometric method to measure enzymatic activity in reactions that generate inorganic pyrophosphate. *Analyt. Biochem.* **243**, 41-45 (1996).

79. Thoden, J. B., Huang, X., Raushel, F. M. & Holden, H. M. Carbamoyl phoshate synthetase: Creation of an escape route for ammonia. *J. Biol. Chem.* **277**, 39722-39727 (2002).

80. Chiu, M., Taurino, G., Bianchi, M. G., Kilberg, M. S. & Bussolati, O. Asparagine synthetase in cancer: Beyond acute lymphoblastic leukemia. *Front. Oncol.* **9**, 1480 (2020).

81. Ikeuchi, H. et al. A human asparagine synthetase inhibitor kills asparaginase-resistant MOLT-4 cells. *Bioorg. Med. Chem.* **20**, 5915-5927 (2012).

82. Zhong, E. D., Bepler, T., Berger, B. & Davis, J. H. CryoDRGN: Reconstructions of heterogeneous cryo-EM structures using neural networks. *Nat. Methods* **18**, 176-185 (2021).

83. Mouilleron, S. & Golinelli-Pimpaneau, B. Conformational changes in ammonia-channeling glutamine amidotransferases. *Curr. Op. Struct. Biol.* **17**, 653-664 (2007).

84. Li, C. et al. Conformational changes of glutamine 5'-phosphoribosylpyrophosphate amidotransferase for two substrate analogue binding: Insight from conventional molecular dynamics and accelerated molecular dynamics simulation. *Front. Chem.* **9**, 640994 (2021).

85. Mouilleron, S., Badet-Denisot, M.-A. & Golinelli-Pimpaneau, B. Glutamine binding opens the ammonia channel and activates glucosamine-6P synthase. *J. Biol. Chem.* **281**, 4404-4412 (2006).

86. Welborn, V. V. & Head-Gordon, T. Computational design of synthetic enzymes. *Chem. Rev.* **119**, 6613-6630 (2019).

87. Guo, H. et al. Electron-event representation data enable efficient cryoEM file storage with full preservation of spatial and temporal resolution. *IUCr J.* **7**, 860-869 (2020).

88. Pettersen, E. et al. UCSF Chimera – A visualization system for exploratory research and analysis. *J. Comput. Chem.* **25**, 1605-1612 (2004).

89. Sanchez-Garcia, R. et al. DeepEMhancer: A deep learning solution for cryo-EM volume post-processing. *Commun Biol* **4**, 874 (2021).

90. Cianfrocco, M. A., Wong-Barnum, M., Youn, C., Wagner, R. & Leschziner, A. in *Proceedings of the Practice and Experience in Advanced Research Computing 2017 on Sustainability, Success and Impact* (Association for Computing Machinery, 2017).

91. Murshudov, G. N., Vagin, A. A. & Dodson, E. J. Refinement of macromolecular structures by the maximum-likelihood method. *Acta Crystallogr. D Biol. Crystallogr.* **53**, 240-255 (1997).

92. Adams, P. et al. PHENIX: A comprehensive Python-based system for macromolecular structure solution. *Acta Crystallogr. D Biol. Crystallogr.* **66**, 213-221 (2010).

93. Emsley, P., Lohkamp, B., Scott, W. G. & Cowtan, K. Features and development of Coot. *Acta Crystallogr. D Biol. Crystallogr.* **66**, 486-501 (2010).

94. Pettersen, E. et al. UCSF ChimeraX: Structure visualization system for researchers, educators, and developers. *Protein Sci.* **30**, 70-82 (2021).

95. Søndergaard, C. R., Olsson, M. H. M., Rostkowski, M. & Jensen, J. H. Improved treatment of ligands and coupling effects in empirical calculation and rationalization of pK_a values. *J. Chem. Theory Comput.* **7**, 2284-2295 (2011).

96. Tesmer, J. J. G., Klem, T. J., Deras, M. L., Davisson, V. J. & Smith, J. L. The crystal structure of GMP synthetase reveals a novel catalytic triad and is a structural paradigm for two enzyme families. *Nat. Struct. Biol.* **3**, 74-86 (1996).

97. Fellner, M., Hausinger, R. P. & Hu, J. A structural perspective on the PP-loop ATP pyrophosphatase family. *Crit. Rev. Biochem. Mol. Biol.* **53**, 607-622 (2018).

98. Johnston, R. C., Yao, K., Kaplan, Z., Chelliah, M., Leswing, K. Seekins, S., Watts, S., Calkins, D., Chief Elk, J., Jerome, J. V., Repasky, M. P. & Shelley, J. C. Epik: pK_a and protonation state prediction through machine learning. *J. Chem. Theory Comput.* **19**, 2380-2388 (2023).

99. Jorgensen, W. L., Chandrasekhar, J., Madura, J., Impey, R. W. & Klein, M. L. Comparison of simple potential functions for simulating liquid water. *J. Chem. Phys.* **79**, 926-935 (1983).

100. Kaminski, G. A., Friesner, R. A., Tirado-Rives, J. & Jorgensen, W. L. Evaluation and reparametrization of the OPLS-AA force field for proteins via comparison with accurate quantum chemical calculations on peptides. *J. Phys. Chem. B* **105**, 6474-6487 (2001).

101. Darden, T., York, D. and Pedersen, L. Particle mesh Ewald: An Nlog(N) method for Ewald sums in large systems. *J. Chem. Phys.* **98**, 10089-10092 (1993).

Acknowledgments

We thank Francesco Ortuso for technical support of the computational studies. The authors would also like to acknowledge the Indiana University School of Medicine EM facility and NIH/NIGMS, S10 OD028723 for supporting this work. Additional funds for the EM structure determinations were provided by the Indiana University School of Medicine (Y.T.), and, in part, NIGMS award number R01GM111695 (Y.T.) and the American Cancer Society award number DBG-23-1038947-01-IBCD (Y.T.). This work was also supported by the CNRS (V.C.), and the French National Research Agency grant number ANR-19-CE11-0023-01 (V.C.). Funding for the computational studies was provided by the Biotechnology and Biological Sciences Research Council, grant number P/0118017/1 (N.G.J.R.), by the European Committee grant number FESR FSE 2014- 2020 (S.A.), and by Regione Calabria (S.A). The kinetics studies were supported by start-up funding from the Florida State University (W.Z.). C.G. was supported by funds from the EU, project number FSE-FESR PON-RI 2014-2020. The content is solely the responsibility of the authors and does not necessarily represent the official views of the Indiana University School of Medicine. The European Committee and Regione Calabria also decline any responsibility concerning the use of the information disclosed in the paper.

Author Contributions

A.C., W.Z., Y.T., S.A. and N.G.J.R. designed the research. Y.T. and M.V. collected data, and Y.T. solved the EM structures. V.C. and Y.T. carried out the 3D variability analysis. A.J.N. performed the kinetic assays under the direction of W.Z. A.C., A.L. and C.G. performed the computer simulations under the guidance of S.A. The MD simulation data were analyzed by A.C., C.G., W.Z. and N.G.J.R. Finally, the paper was co-written by W.Z., Y.T. and N.G.J.R. with input from all other authors.

Competing Interests

The authors declare no competing interests. The funders had no role in the design of the study; in the collection, analyses, or interpretation of data; in the writing of the manuscript, or in the decision to publish the results.

FIGURES

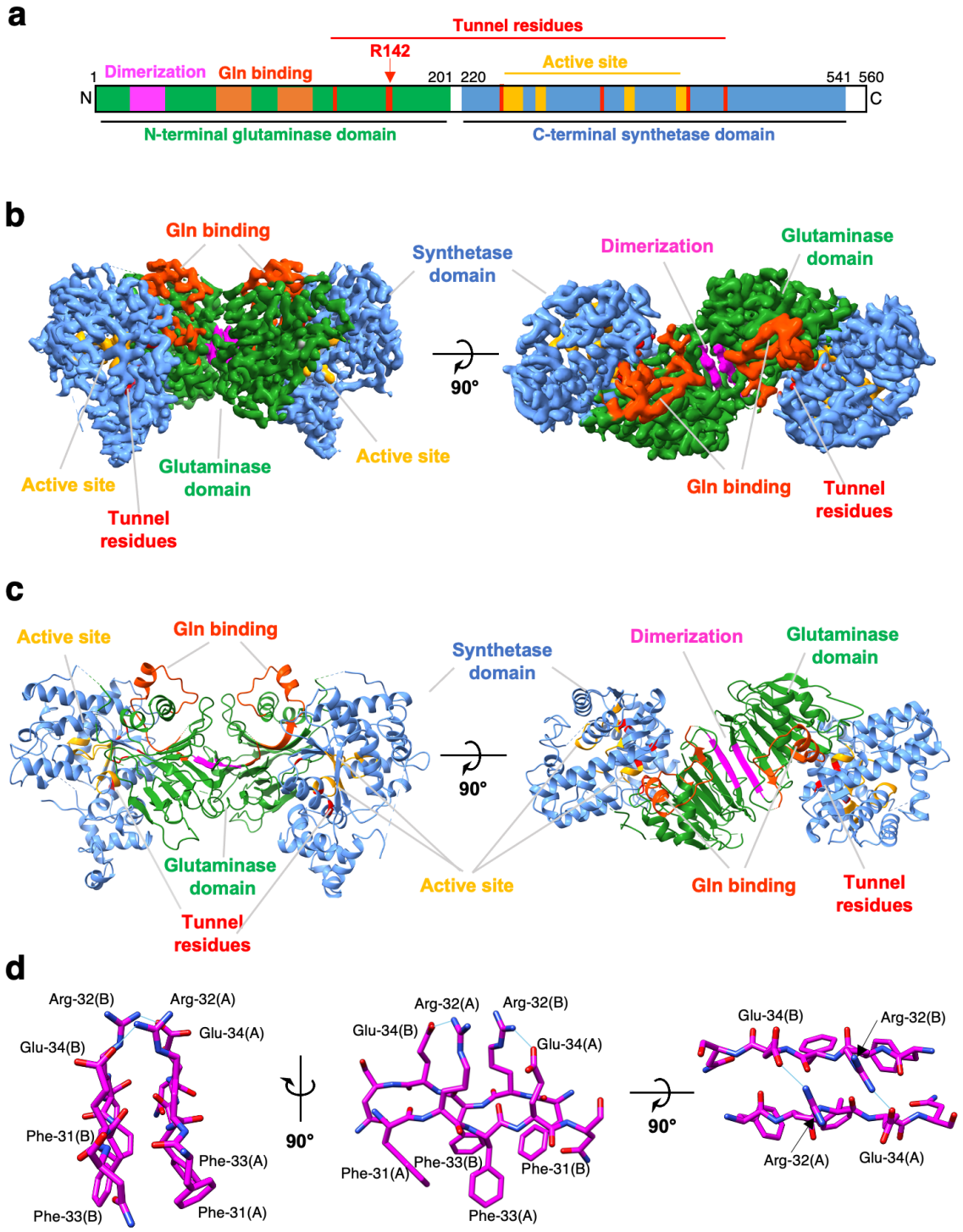

Fig. 1. | Cryo-EM structure of human ASNS. **a** Schematic representation showing the N-terminal glutaminase (forest green), dimerization (magenta) and the C-terminal synthetase (cornflower blue) domains. The glutamine-binding (orange red) and synthetase active site (orange) are also indicated together with residues constituting the intramolecular tunnel (red). **b** EM map and **c** ribbon representation of human ASNS (coloring is identical to that used in **a**). **d** Close-up view of the dimerization motif showing residues (C, magenta; N, blue, O, red) participating in salt bridges (shown by cyan lines), and hydrophobic interactions. (A): monomer A; (B): monomer B.

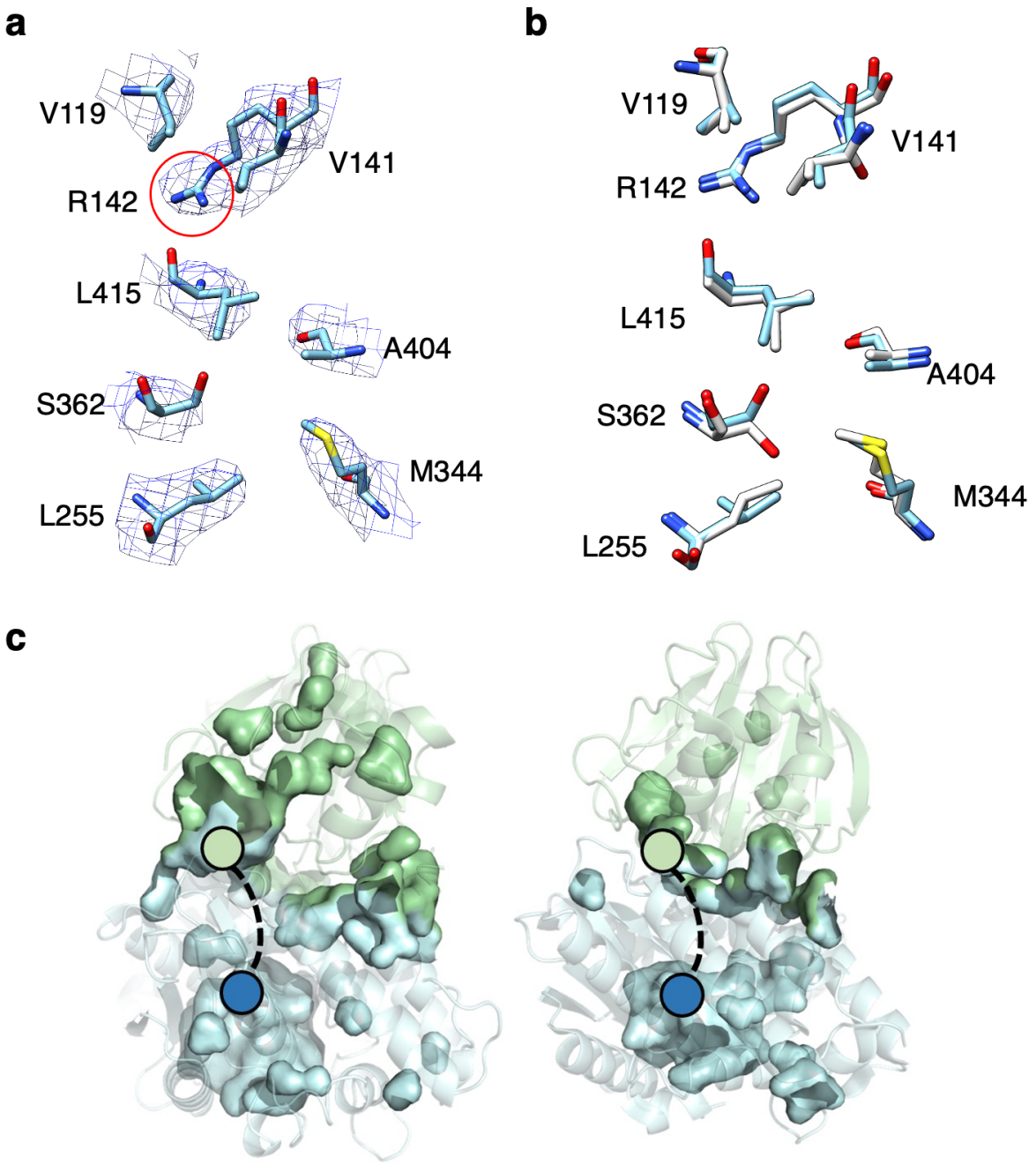

Fig. 2. | **a** Residues defining the intramolecular tunnel in the EM structure of WT ASNS with corresponding densities. Residues V119, V141, R142, L255, M344, S362, A404, and L415 are colored in sky blue and EM density (mesh) in blue. **b** Superimposition of residues defining the intramolecular tunnel in the EM (colored sky blue as in Fig. 1a) and X-ray (white) structures of human ASNS. **c** Internal cavity and pocket representations, as computed by PyMol, showing the discontinuous tunnels in the EM (left) and X-ray (right) structures. The N- and C-terminal domains of both structures are colored green and blue, respectively, with colored circles showing the two active sites. Dashed lines connecting the active sites represent the position of the open tunnel seen in the X-ray crystal structure of the bacterial enzyme (Supplementary Fig. S13).

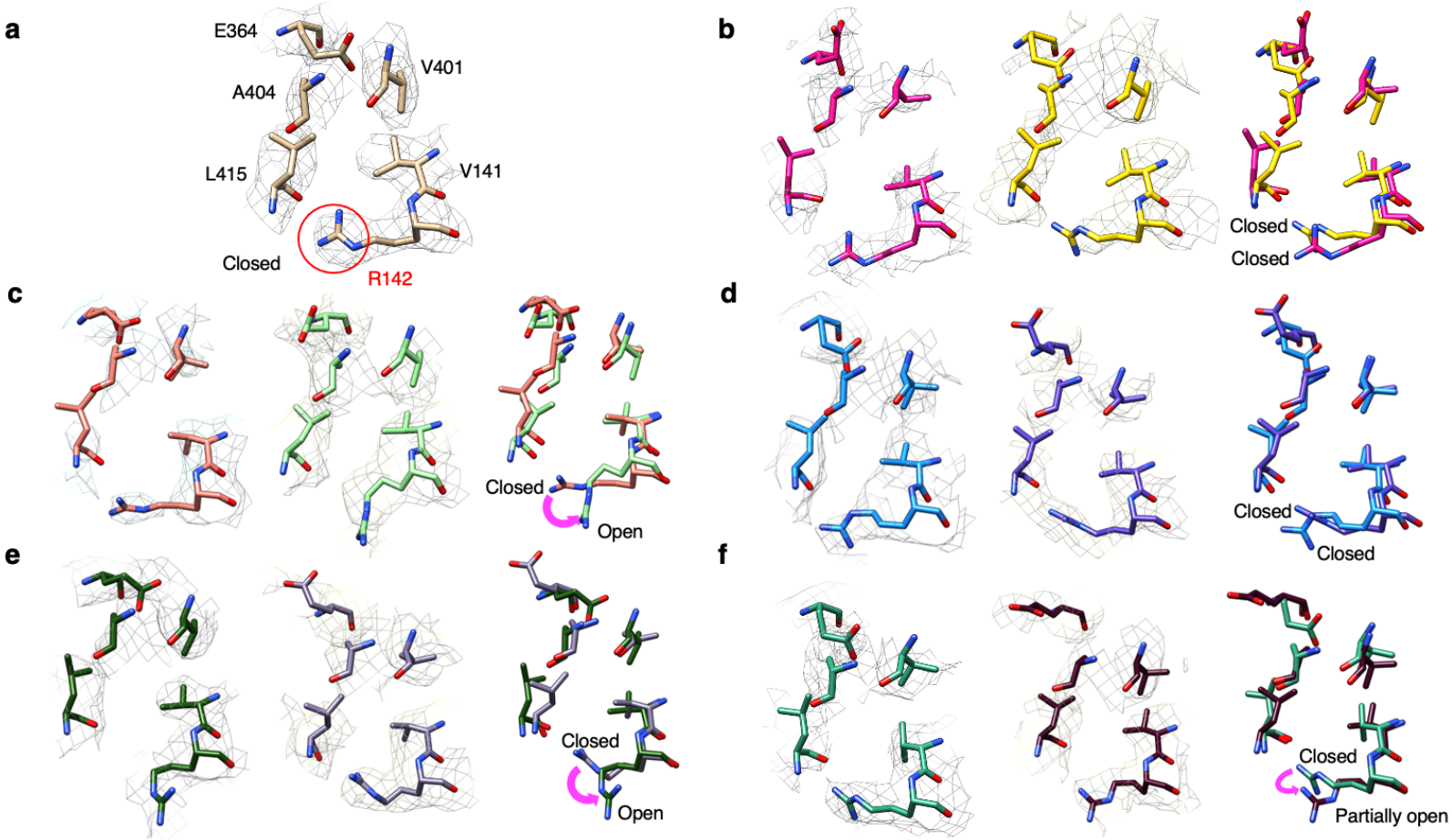

Fig. 3. | PCA-derived structures of the ammonia tunnel in human ASNS obtained from 3D variability analysis. **a** Side view of critical residues (Val-141, Arg-142, Glu-364, Val-401, Ala-404, Val-414, Leu-415) constituting the ammonia tunnel derived from the consensus EM map. The side chain of Arg-142 that blocks the tunnel is indicated (red circle). Side view of critical residues constituting ammonia tunnel derived from the variable EM maps derived from 3DVA and corresponding models generated by 3D variable refinement. Critical residues constituting ammonia tunnel derived from the maps at frame 1 (one end) and frame 20 (the other end) are superimposed: **b** PCA component 0, **c** PCA component 1, **d** PCA component 2, **e** PCA component 3, **f** PCA component 4.

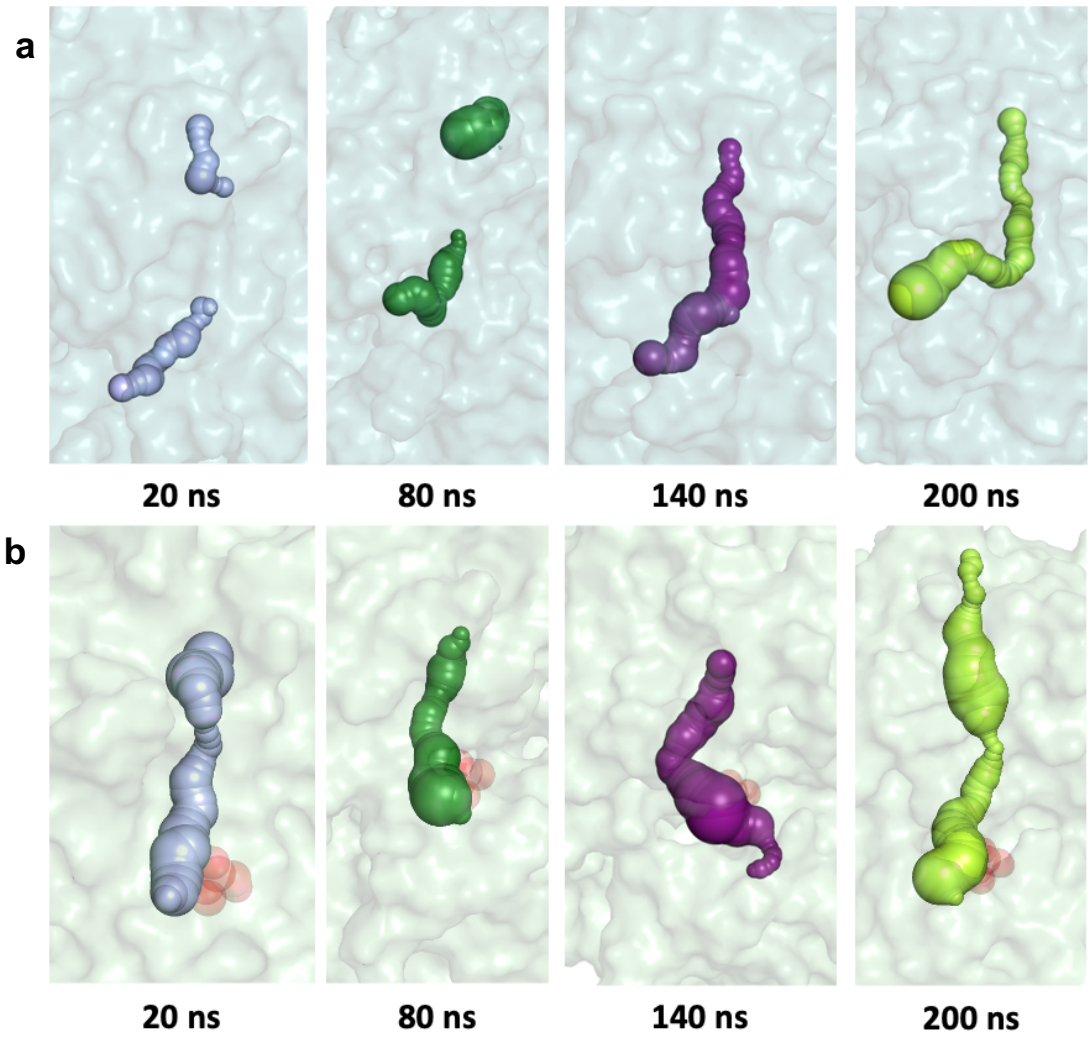

Fig. 4. | Snapshots from the MD trajectories computed for **a** the human apo-ASNS and **b** the human R142I ASNS variant. Proteins in **a** and **b** are shown as surfaces in light cyan and light green, respectively. Red spheres indicate the position of the side chain of Ile-142. The surface of the tunnel is indicated by spheres (t = 20 ns, light purple; t = 80 ns, forest green; t = 140 ns, violet purple; t = 200 ns, lime). Tunnels were identified using the CAVER 3.0 software package[75] and rendered in PyMol.

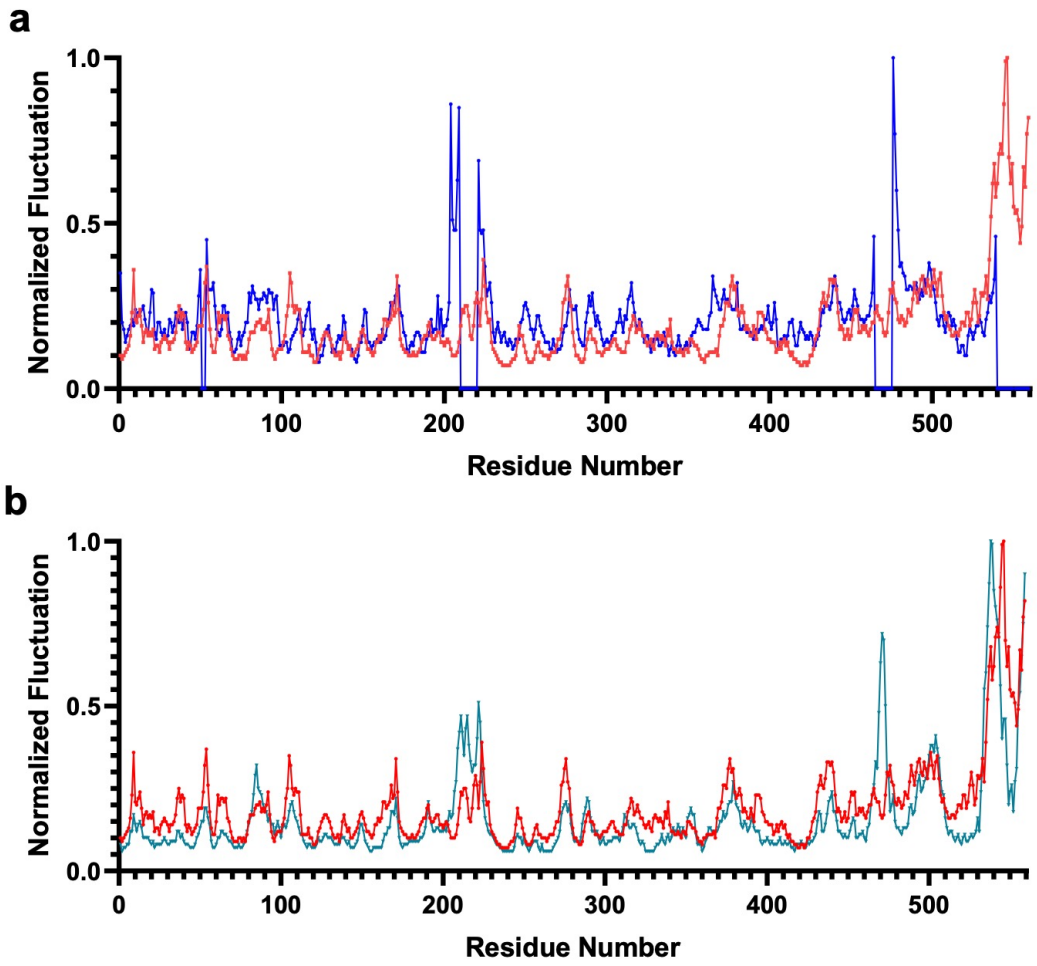

Fig. 5. | Normalized RMSF values for residues in human ASNS. **a** Comparison of values from the 100 3DVA-derived structures of chain A (blue) and the MD trajectory of apo-ASNS (red). **b** Comparison of values from the MD trajectories of apo-ASNS (red) and the human ASNS/β-aspartyl-AMP/$MgPP_i$ ternary complex (teal).

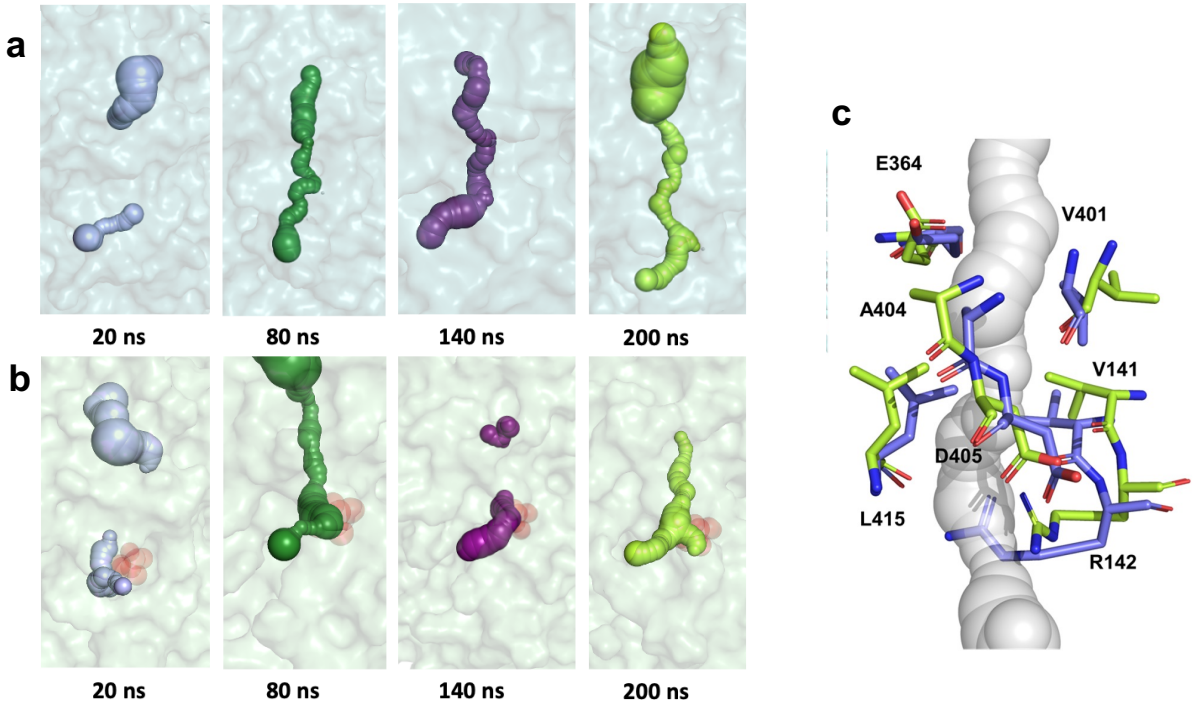

Fig. 6. | Snapshots from the MD trajectories computed for the ternary complexes of **a** human apo-ASNS and **b** the human R142I ASNS variant. Proteins in **a** and **b** are shown as surfaces in light cyan and light green, respectively. Red spheres indicate the position of the side chain of Ile-142. The surface of the tunnel is indicated by spheres (t = 20 ns, light purple; t = 80 ns, forest green; t = 140 ns, violet purple; t = 200 ns, lime). Tunnels were identified using the CAVER 3.0 software package[75] and rendered in PyMol. **c** Superimposed snapshots from the MD trajectory of the human ASNS/b-aspartyl-AMP/$MgPP_i$ ternary complex showing the reorientation of the Arg-142 side chain (carbons are colored in slate (t = 0 ns) or slate (t = 200 ns), and oxygen and nitrogen atoms are colored red and blue, respectively).

TABLE 1 Steady-state kinetic parameters for WT human ASNS and the two variants

Nitrogen Source	L-Glutamine				Ammonia	
Enzyme	$^{app}K_M$ (Asp) mM	k_{cat} s^{-1}	$^{app}K_M$ (Gln) mM	k_{cat} s^{-1}	$^{app}K_M$ (NH_3) mM	k_{cat} s^{-1}
WT	0.24 ± 0.03	0.8 ± 0.1	0.90 ± 0.08	0.50 ± 0.03	0.3 ± 0.2	0.6 ± 0.1
R142I	0.10 ± 0.02	0.18 ± 0.01	0.01 ± 0.003	0.06 ± 0.002	0.11 ± 0.03	0.40 ± 0.01
R142A	0.20 ± 0.03	0.4 ± 0.1	0.03 ± 0.02	0.10 ± 0.02	0.6 ± 0.1	0.7 ± 0.1